Atmospheric Research 245 (2020) 105075

Contents lists available at ScienceDirect

Atmospheric Research

journal homepage: www.elsevier.com/locate/atmosres

An improved hydrometeor identification method for X-band dual-polarization radar and its application for one summer Hailstorm over Northern China

Chuanhong Zhao[a,b,*], Yijun Zhang[a,c], Dong Zheng[d], Yunjun Zhou[b,*], Hui Xiao[e], Xiaoling Zhang[f]

[a] Department of Atmospheric and Oceanic Sciences & Institute of Atmospheric Sciences, Fudan University, Shanghai 200438, China
[b] Plateau Atmosphere and Environment Key Laboratory of Sichuan Province, College of Atmospheric Science, Chengdu University of Information & Technology, Chengdu 610225, China
[c] CMA-FDU Joint Laboratory of Marine Meteorology, Shanghai 200438, China
[d] Laboratory of Severe Weather, Chinese Academy of Meteorological Sciences, Beijing 100089, China
[e] Key Laboratory of Cloud-Precipitation Physics and Severe Storms, Institute of Atmospheric Physics, Chinese Academy of Sciences, Beijing 100029, China
[f] Beijing Meteorological Information Center, Beijing 100089, China

ARTICLE INFO

Keywords:
Hailstorm
Hydrometeor identification
X-band dual-polarization radar

ABSTRACT

Currently, high-resolution severe storm observations obtained by vehicle-mounted mobile X-band dual-polarization radar (X-pol) are widely used in severe storm structure and dynamics studies; however, the identification of hailstones based on X-pol is still rare, leading to the limited application of X-pol in identifying hydrometeors in the microphysical processes of severe storms. Based on previous works, this study constructs an improved X-pol hydrometeor identification (HID) method for hailstorms; the hydrometeor categories include a rain-hail mixtures (RH) category indicating hailstones are melting or experiencing wet growth, and the correlation coefficient between horizontally and vertically polarized echoes (ρ_{HV}) is used to locate the local mixed phase region in storms to avoid misclassifications of hydrometeors resulted by environmental temperature in this local mixed phase region. The improved HID method can see liquid water information above the melting layer; it provides a possibility to observe the microphysical process of hailstones wet growth above the melting layer. Furthermore, this improved HID method was utilized to study the high spatiotemporal resolution data collected by the Institute of Atmospheric Physics of Chinese Academy of Sciences (IAP) X-pol for one summer hailstorm over northern China. The results indicate that the identified RH is consistent with the surface hail record of National weather observatory of China Meteorological Administration (CMA), the specific differential phase (K_{DP}) column is more sensitive than the differential reflectivity (Z_{DR}) column for indicating the updraft zone movement, and we considered that the relative position between the key area of hail (KAH, where above the Z_{DR} column, $Z_{DR} \sim -2$ to 0 dB, $Z_H \sim \geq 50$ dBZ) and the updraft zone (indicated by the Z_{DR}, K_{DP} column) will determine the evolution of hail. Furthermore, high-density graupels (HDGs) in the upper layer of the KAH may be the source of RH embryos, and these HDGs collect liquid droplets from the liquid water-rich (LWR) area located behind the KAH to form a large number of RH in the lower layer of the KAH. These characteristics are important for hailstone forecasting and warnings.

1. Introduction

Polarimetric radar can identify hydrometeors in severe storms according to polarization parameters (horizontal reflectivity (Z_H); differential reflectivity (Z_{DR}); specific differential phase (K_{DP}) and the correlation coefficient between horizontally and vertically polarized echoes (ρ_{HV})) (e.g., Bringi and Chandrasekar, 2001; Chandrasekar et al., 2011; Dolan and Rutledge, 2009; Hall et al., 1980; Keenan, 2003; Kouketsu et al., 2015; Lim et al., 2005; Liu and Chandrasekar, 2000; Marzano et al., 2006, 2008; Park et al., 2009; Snyder et al., 2010; Straka et al., 2000; Thompson et al., 2014; Zrnic and Ryzhkov, 1999). Many earlier hydrometeor identification (HID) works are proposed based on

Abbreviations: X-pol, X-band dual-polarization radar; HID, hydrometeor identification; RH, rain-hail mixtures; IAP, the Institute of Atmospheric Physics; CMA, China Meteorological Administration; KAH, the key area of hail; HDGs, high-density graupels; LWR, liquid water-rich

* Corresponding authors at: College of Atmospheric Science, Chengdu University of Information & Technology, 24 Xuefu Road, Chengdu 610225, China.
E-mail addresses: 19113020022@fudan.edu.cn (C. Zhao), zhouyj@cuit.edu.cn (Y. Zhou).

https://doi.org/10.1016/j.atmosres.2020.105075
Received 2 February 2020; Received in revised form 24 April 2020; Accepted 29 May 2020
Available online 30 May 2020
0169-8095/

S/C-band polarimetric radar (e.g., Keenan, 2003; Lim et al., 2005; Liu and Chandrasekar, 2000; Marzano et al., 2006, 2008; Park et al., 2009 and other more; Zrnić et al., 2001); in the last decade, several HID methods for X-band dual-polarization radar (X-pol) have been proposed due to the increasing usage of X-pol (e.g., Bechini and Chandrasekar, 2015; Dolan and Rutledge, 2009; Kouketsu et al., 2015; Snyder et al., 2010; Thompson et al., 2014). Dolan and Rutledge (2009) developed an HID method applicable to X-pol based on **T**-matrix scattering simulations, which can identify seven kinds of hydrometeors: drizzle/light rain, rain, aggregates, ice crystals, low-density graupel, high-density graupel and vertically aligned ice, but in terms of severe storms, this scheme lacks hail identification. Snyder et al. (2010) adapted the S-pol HID method (Park et al., 2009) for use with X-pol based on disdrometer observations and **T**-matrix scattering simulations with idealized drop size distributions and attempted to identify big drops, light-to-moderate rain, heavy rain, and rain-hail mixtures (RH) (the hailstones are melting or experiencing wet growth) well located below the melting level. Although this HID method includes hailstones identification, it lacks identification of ice phase particles above the melting layer. Subsequently, although there are also studies based on the S-pol HID method (Liu and Chandrasekar, 2000) and/or X-pol HID methods (Dolan and Rutledge, 2009; Snyder et al., 2010) to modify HID methods for X-pol to identify hydrometeors in winter storms (e.g., Kouketsu et al., 2015; Thompson et al., 2014) or convection precipitation in May (Oklahoma) (Bechini and Chandrasekar, 2015), currently, identification of hydrometeors in summer hailstorms based on X-pol is still rare, especially in China. There is a large disadvantage in using the above HID methods, which is the choice of environmental temperature parameter (T). T is added as one of a few factors to the HID method because it can separate the liquid precipitation from solid hydrometeors to avoid visible identification errors at the radar sampling volume (e.g., Bechini and Chandrasekar, 2015; Dolan and Rutledge, 2009; Kouketsu et al., 2015; Park et al., 2009; Thompson et al., 2014 and others). Temperature vertical profile is generally available from soundings of adjacent meteorological observation stations or real-time in situ soundings. However, the data of real-time in situ soundings are difficult to acquire, and the early warning time will be reduced; therefore, soundings of adjacent meteorological observation stations are the main way to obtain environmental temperature. For severe storms, liquid drops still exist above the environmental 0 °C layer due to nontransient freezing properties (e.g., Johnson and Hallett, 1968; Smith et al., 1999), or the updraft caused local positive temperature disturbances, or condensation and freezing (melting and evaporation) of hydrometeors caused local positive (negative) temperature disturbances. These characteristics form a local mixed phase region above the melting layer in storms. Therefore, utilizing the environmental temperature of adjacent meteorological observation stations as one parameter of the HID method to separate liquid precipitation from solid hydrometeors within this local mixed phase region is not realistic, and this may cause considerable identification errors. Bechini and Chandrasekar (2015) proposed that using of a parabolic weight for the temperature is intended to exploit the temperature information to minimize misclassifications in regions far from phase transitions and to rely more on radar information to discriminate near the melting layer. ρ_{HV} is the correlation coefficient between the backscattered returns at horizontal and vertical polarizations with zero lag time, and this coefficient is sensitive to the diversity of hydrometeor sizes, shapes, orientations and dielectric constants within the radar sampling volume (Balakrishnan and Zrnić, 1990). ρ_{HV} is usually given a lower weight value because of its fuzzy ability to identify hydrometeors in HID methods; however, ρ_{HV} will decrease significantly ($\rho_{HV} < 0.9$) when the electromagnetic wave passes through a local mixed phased region with large and wet particles in storms; and ρ_{HV} will also show the value between 0.90 and 0.97 when dry ice particles melting. These suggests ρ_{HV} has the ability to mark the local mixed phased region within severe storms (Bringi and Chandrasekar, 2001; Bringi et al., 1997; Giangrand et al., 2008; Kumjian et al., 2010). For example, Stolzenburg et al. (2015) indicated that there is a clear "ρ_{HV} cap" ($Z_H \sim > 45$ dBZ, $\rho_{HV} \sim < 0.9$) above the environmental 0 °C layer within Florida storms in X-pol observations during the initial electrification phase, which means that the depolarization is indicative of a variety of irregularly shaped ice and liquid particles with random orientations in the local mixed phase region. At the beginning of the initial electrification phase (4.0 min before first flash), the ρ_{HV} cap was just above the environmental 0 °C layer ($\rho_{HV} < 0.9$, $Z_{DR} > 0$), it indicated this is a local mixed phase region comprised of various shapes and orientations of ice, drops, and then, within a minute (3.3 min before first flash), the ρ_{HV} cap rapidly strengthened and extended below the 0 °C layer, the corresponding Z_{DR} values decreased from positive values to negative values through 0 °C layer, this ρ_{HV} cap indicated a local mixed phase region comprised of various ice shapes and orientations, freezing drops, and then, one minute later (2.3 min before first flash), the minimum value of ρ_{HV} cap dropped to 0.8, and the relative minima in Z_{DR} within the severe storm core ($Z_H \sim 60$ dBZ) at this time indicated that vertically elongated graupel and hail, freezing drops were present. The ρ_{HV} cap at this time indicated a local mixed phase region comprised supercooled, freezing drops; irregular hail and graupel.

In addition, one of the most notable polarized signal features in severe storms is called the Z_{DR} column, and extensive observational and simulation studies indicated that this column comprises large raindrops and smaller wet ice particles and always marks the main updraft zone and hail growth area within storms (e.g., Bringi et al., 1991, 1996, 1997; Caylor and Illingworth, 1987; Conway and Zrnić, 1993; Hall et al., 1980, 1984; Illingworth et al., 1987; Kumjian et al., 2010, 2014; Raghavan and Chandrasekar, 1994; Ryzhkov et al., 1994; Smith et al., 1999; Snyder et al., 2015, 2017b; Vivekanandan et al., 1990; Wakimoto and Bringi, 1988). A Z_{DR} column is usually defined as a narrow zone of positive Z_{DR} values (i.e., $Z_{DR} \geq 1$ dB) in the vertical direction above the environmental 0 °C layer. Similar to the Z_{DR} column, the "K_{DP} column" is a zone of positive K_{DP} values above the 0 °C layer; however, many current studies on K_{DP} columns are not uniform (Hubbert et al., 1998; Kumjian and Ryzhkov, 2008; Loney et al., 2002; Snyder et al., 2017b; Zrnić et al., 2001). The K_{DP} column contains a large amount of liquid water, and its size is closely related to the updraft intensity during storms. However, there is a study suggesting that the hail content in storms is highly correlated with the size of the K_{DP} column (Snyder et al., 2017b).

At present, there has been widespread interest in collecting high spatiotemporal resolution data by polarimetric radar in severe storms for studying the structure and dynamics of severe storms. One way to achieve a finer resolution is using mobile radar to move closer to the storm and selecting an appropriate scanning strategy. Therefore, the phenomenon of utilizing vehicle-mounted mobile polarimetric radar to observe severe storms is increasing (Hu et al., 2012; Kumjian et al., 2010; Xue, 2016). In recent years, mobile X-pol has been increasingly used in the observations of precipitation systems because of its small size, relatively low cost, and convenience for mobile detection, e.g., the University of Massachusetts "UMass X-pol" (Bluestein et al., 2007a, 2007b; Snyder et al., 2010, 2013), the National Severe Storms Laboratory/University of Oklahoma polarimetric X-band Experimental Radar for the Examination of Storms (XERES; see Melnikov et al., 2009), the University of Oklahoma "RaX-pol" (Pazmany et al., 2013; Snyder et al., 2017b), and the Institute of Atmospheric Physics of Chinese Academy of Sciences "IAP X-pol" (He et al., 2009a, 2009b, 2010). Notably, the polarization parameters of polarimetric radar will change significantly with varying wavelengths (Bringi and Chandrasekar, 2001). For example, hailstones in X-pol will produce a weaker echo intensity than S-pol due to the presence of non-Rayleigh scattering; therefore, special attention should be used when using X-pol to distinguish the polarization characteristics from those of S-pol. Recently, in studying the polarization characteristics of X-pol in supercell observations (Snyder et al., 2013, 2017a), it was found that X-pol plays

a role in the observations of large-scale ice particles such as hailstones, but how do the polarization parameters of X-pol indicate the generation and extinction of hailstones? Focusing on the above issues, this study takes IAP X-pol (see Section 3 for more details) as the research object to construct an improved HID method that can avoid the misclassification in a local mixed phase region within storms resulted by environmental temperature and include the RH category for trying to observe the microphysical process of hailstones wet growth above the melting layer (details in Section 2), and a simple verification of the RH category results below the melting layer was performed (details in Section 4). In addition, relationships between hailstones and the Z_{DR}, K_{DP} column and other storm characteristic parameters were discussed based on the HID results (in Section 4). A summary is also included in Section 5. The results of this study show the potential for X-pol radar to monitoring and early warnings of hail storms.

2. Construction of the HID method

The construction of the HID method based on the fuzzy logic algorithm and the framework of fuzzy logic-based HID methods has been widely used in the last decade, and the fuzzy logic algorithm is easier to implement and modify than other methods, including Boolean trees, classical statistical decision theory, and neural networks, and the HID method has the ability to identify hydrometeors affected by noise and overlapping threshold detection data (e.g., Liu and Chandrasekar, 2000; Park et al., 2009; Straka et al., 2000; Vivekanandan et al., 1999). This method contains the following three modules.

2.1. Input variables

Four radar polarization parameters (Z_H, Z_{DR}, K_{DP}, ρ_{HV}) and the environmental temperature parameter (T) are used as input parameters for hydrometeor identification. For RH identification, an additional LK_{DP} parameter ($LK_{DP} = 10\log(K_{DP})$) is introduced.

For avoiding misclassifications of hydrometeors resulted by environmental temperature in the local mixed phase region, identifying hydrometeors only relies on radar information in this local mixed phase region. In addition, temperature information is exploited to minimize misclassifications in regions except from the local mixed phase region. According to previous statistical studies on polarization characteristics (Bringi and Chandrasekar, 2001; Bringi et al., 1997; Dolan and Rutledge, 2009; Giangrand et al., 2008; Keenan, 2003; Kumjian et al., 2010), ρ_{HV} is used for locating the local mixed phase region within storms. The relatively low ρ_{HV} values (< 0.98) within the core of hailstorms ($Z_H \sim \geq$ 30 dBZ) are divided into two categories: I) $\rho_{HV} < 0.9$, which indicates more complex local mixed phase regions (such as more large rain droplets, rain-hail mixtures, and HDGs experiencing wet growth); and II) $0.9 \leq \rho_{HV} \leq 0.98$, which indicates a relatively simple local mixed phase region (diameters of particles are smaller than large particles such as hailstones, and low ρ_{HV} (0.9–0.98) is mainly due to the presence of supercooled water or various shapes and orientations of ice). Type II is mainly caused by relative smaller particles than Type I, which is most likely above the environmental 0 °C layer, so type II is limited to altitudes higher than the environmental 0 °C layer, while hailstones in type I, are conducive to low ρ_{HV} (< 0.9) below the 0 °C layer; therefore, it is not limited. In this way, the local mixed phase region in the entire core area of storms can be marked by ρ_{HV}. In the local mixed phase region, the environmental temperature is no longer added to infer the phases of particles but only relying on polarization parameters for hydrometeor identification. Therefore, the misclassification in a local mixed phase region resulted by environmental temperature will be avoided.

2.2. Hydrometeor categories

This study constructs an improved X-pol hydrometeor identification scheme based on Dolan and Rutledge (2009) and Snyder et al. (2010), including the following eight hydrometeor types: 1) drizzle rain (DZ), 2) rain (RN), 3) aggregates (AG), 4) ice crystals (CR), 5) low-density graupel (LDG), which is expected in relatively cold regions of storms (−10 °C to −20 °C), 6) high-density graupel (HDG), which is growing in regions of large supercooled water contents, melting graupel, and freezing of supercooled rain are all processes that promote graupel of greater bulk density compared to LDG, 7) vertically aligned ice (VI) and 8) rain-hail mixture (RH). Among these types, as Straka et al. (2000) noted, graupel and small hail have similar characteristics; therefore, Dolan and Rutledge (2009) chosen to group these two hydrometeor types into one category. The RH which above the melting layer are likely to contain hailstones that are experiencing wet growth (Dolan and Rutledge, 2009; Keenan, 2003; Straka et al., 2000). These hydrometeors roughly cover the types of particles seen in severe storms.

2.3. Membership functions

The membership function of this study is a trapezoidal asymmetric function (see details in Park et al. (2009)). Membership function settings of DZ, RN, CR, AG, LDG, HDG and VI use Dolan and Rutledge (2009) theory-based hydrometeor polarization parameter threshold ranges, and the membership function setting of RH adopts the scheme used in Snyder et al. (2010). Table 1 shows the membership function settings corresponding to each parameter (the setting of T mainly follows that of Dolan and Rutledge (2009), and the temperature threshold

Table 1
Membership function parameters used for the X-pol variables in this paper (the RH membership functions for Z_{DR} and LK_{DP} are two-dimensional functions of Z_H: $A1 = 3.2 \times 10^{-5} Z_H^3$–$0.0017 Z_H^2 + 0.042 Z_H$-0.39, $B1 = 0.7Z_H$-42, from Snyder et al. (2010)).

		$x1$	$x2$	$x3$	$x4$
Z_H	GC/AP	15	20	70	80
	DZ	−27	−27	31	31
	RN	25	25	59	59
	CR	−25	−25	19	19
	AG	−1	−1	33	33
	LDG	24	24	44	44
	HDG	32	32	54	54
	VI	−25	−25	32	32
	RH	40	45	65	70
Z_{DR}	GC/AP	−4	−2	1	2
	DZ	0.0	0.0	0.9	0.9
	RN	0.1	0.1	5.6	5.6
	CR	0.6	0.6	5.8	5.8
	AG	0.0	0.0	1.4	1.4
	LDG	−0.7	−0.7	1.3	1.3
	HDG	−1.3	−1.3	3.7	3.7
	VI	−2.1	−2.1	0.5	0.5
	RH	−1.0	0.0	$A1$	$A1 + 0.5$
LK_{DP}	GC/AP	−30	−25	10	20
	RH	−10	−4	$B1$	$B1 + 1$
K_{DP}	DZ	0.0	0.0	0.06	0.06
	RN	0.0	0.0	25.5	25.5
	CR	0.0	0.0	0.3	0.3
	AG	0.0	0.0	0.4	0.4
	LDG	−1.4	−1.4	2.8	2.8
	HDG	−2.5	−2.5	7.6	7.6
	VI	−0.15	−0.15	0.0	0.0
ρ_{HV}	GC/AP	0.5	0.6	0.9	0.95
	DZ	0.985	0.985	1	1
	RN	0.98	0.98	1	1
	CR	0.97	0.97	1	1
	AG	0.978	0.978	1	1
	LDG	0.985	0.985	1	1
	HDG	0.965	0.965	1	1
	VI	0.93	0.93	1	1
	RH	0.8	0.85	0.95	1.0
SD(Z_H)	GC/AP	2	6	15	20
SD(φ_{DP})	GC/AP	20	30	50	60

setting of RH refers to that of Keenan (2003)). In addition, the setting of the membership function of ground clutter and anomalous propagation (GC/AP) is consistent with Snyder et al. (2010), where SD(Z_H) and SD (φ_{DP}) are defined as follows:

$$SD(Z_H) = \sqrt{\frac{\sum_{1km} [Z_H - mean(Z_H)]^2}{n_Z}}, \quad (1)$$

$$SD(\varphi_{DP}) = \sqrt{\frac{\sum_{2km} [\varphi_{DP} - mean(\varphi_{DP})]^2}{n_\varphi}}, \quad (2)$$

where the *mean* in Eqs. (1) and (2) indicates the average of the Z_H and φ_{DP} parameters with window lengths of 1 km and 2 km, respectively, and n represents the number of corresponding range bins. The HID score is calculated as follows (using the scoring method in Park et al. (2009)):

$$S_i = \frac{\sum_{j=1}^{7} W_{ij} Q_j P^{(i)}(V_j)}{\sum_{j=1}^{7} W_{ij} Q_j}, \quad (3)$$

where i is the output type of the hydrometeor, j is the input variable, Q_j is the confidence factor of the j-th input variable (see Park et al. (2009) for details), $P^{(i)}(V_j)$ is the membership function, S_i is the score, and W_{ij} is the weight (Table 2, wherein the weights of the radar polarization parameters for RN, CR, AG, LDG, HDG, and VI follow those of Dolan and Rutledge (2009), and the weights of the radar polarization parameters for RH and GC/AP follow those of Park et al. (2009)). The final identification of hydrometeor type is based on the maximum value in the score. Any score that is equal or judged to be GC/AP is identified as an unclear classification (UC).

3. Radar and data

The IAP X-pol vehicle-mounted mobile radar belongs to the Institute of Atmospheric Physics of the Chinese Academy of Science (IAP). The radar is located in the Shunyi District (40.18°N, 116.68°E) when the hailstorm is observed in this study; for more details about the IAP X-pol, see Table 3. In the past decade, there have been some studies on convective storms based on IAP X-pol observations (e.g., Feng et al., 2016, 2018, 2019; Guo et al., 2015; He et al., 2009a, 2009b, 2010; Tang et al., 2014; Zhao et al., 2019). X-pol can detect polarization parameters such as Z_H, Z_{DR}, φ_{DP} (K_{DP}), ρ_{HV}, and so on. For these parameters, a preprocess for radar data quality control is required. Firstly, Z_{DR} bias should be corrected (Bringi and Chandrasekar, 2001; Feng et al., 2018, 2019), φ_{DP} is smoothed following previous studies (Hu and Liu, 2014; Zhao et al., 2019), then the value of K_{DP} is calculated from φ_{DP} by piecewise linear regression using a least squares fit over an interval that varies with the level of Z_H following Wang and Chandrasekar (2009). Values of Z_H and Z_{DR} below the melting layer are corrected for rainfall attenuation following Park et al. (2005a, 2005b), also, ρ_{HV} is corrected using SNR

Table 2
Weights for input variables.

Hydrometeor types	Z_H	Z_{DR}	K_{DP}	LK_{DP}	ρ_{HV}	T	SD(Z_H)	SD(φ_{DP})
UC(GC/AP)	0.2	0.4	0	0	1	0	0.6	0.8
DZ	1.5	0.4	1	0	0.2	0.5	0	0
RN	1.5	0.4	1	0	0.2	0.5	0	0
CR	1.5	0.4	1	0	0.2	0.5	0	0
AG	1.5	0.4	1	0	0.2	0.5	0	0
LDG	1.5	0.4	1	0	0.2	0.5	0	0
HDG	1.5	0.4	1	0	0.2	0.5	0	0
VI	1.5	0.4	1	0	0.2	0.5	0	0
RH	1.5	0.4	0	1	0.2	0.5	0	0

Table 3
Characteristics of the IAP X-pol radar.

IAP X-pol radar	
Physical characteristics	
Operating frequency	9.37 GHz
Antenna diameter	2.4 m
Antenna 3-dB beam width	1°
Transmission characteristics	
Peak power	75 kW
Pulse length	0.5 μs
Range resolution	150 m
Location characteristics	
Altitude	26.1 m
Location	40.18°N, 116.68°E

following Schuur et al. (2003). The radar data are interpolated into a Cartesian grid with a resolution of 0.15 km × 0.15 km in both the horizontal and vertical directions.

The analytical data of the IAP X-pol observations in this study are derived from one severe storm on 5 August 2017 over northern China, and this storm produced surface hail. IAP X-pol is located in Shunyi, Beijing (red pentagram in Fig. 1). The Huairou (HR) station (black cross in Fig. 1, 40.36°N, 116.63°E), which is the National Weather Observatory of the China Meteorological Administration (CMA) and the severe weather spotter of the HR station, recorded information on surface hail during this hailstorm. Daxing (DX) station (blue triangle in Fig. 1, 39.93°N, 116.28°E), which is the National Weather Observatory of the CMA, provides environmental temperature information at 1200:00 (all times in this study are converted to universal time coordinated (UTC)) on 5 August 2017. The time period of IAP X-pol observations covers the period of surface hail observations recorded at HR station (Plane Position Indicators (PPIs) of IAP X-pol: 1141:18 to 1208:00; Range Height Indicators (RHIs) of IAP X-pol: 1145:55 to 1211:48). To track the core of this hailstorm and obtain high spatio-temporal resolution radar data (RHIs) in the vertical direction, operators of IAP X-pol only select a short-term PPI scan with a 4° elevation angle to determine the azimuth angle of the RHI scan as soon as possible, which shortens the time interval of RHIs by approximately 2 to 3 min. This will help us to observe and study the short-term continuity changes in the core of this hailstorm.

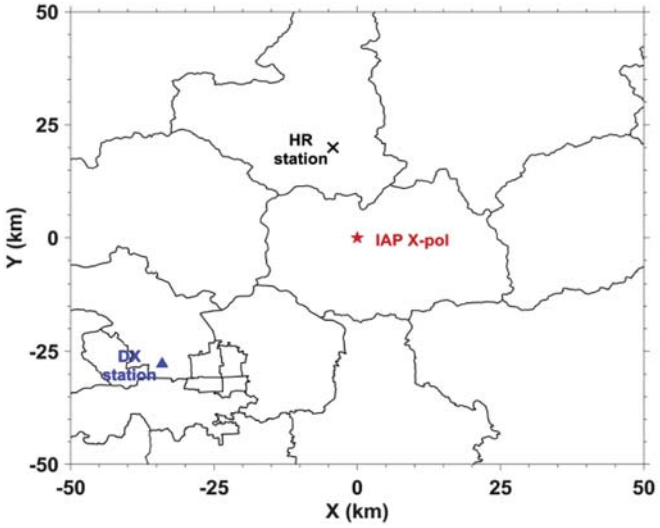

Fig. 1. The map shows the location of the IAP X-pol (red pentagram) and the National Weather Observatory of the China Meteorological Administration (Huairou (HR) station, black cross; Daxing (DX) station, blue triangle). (For interpretation of the references to colour in this figure legend, the reader is referred to the web version of this article.)

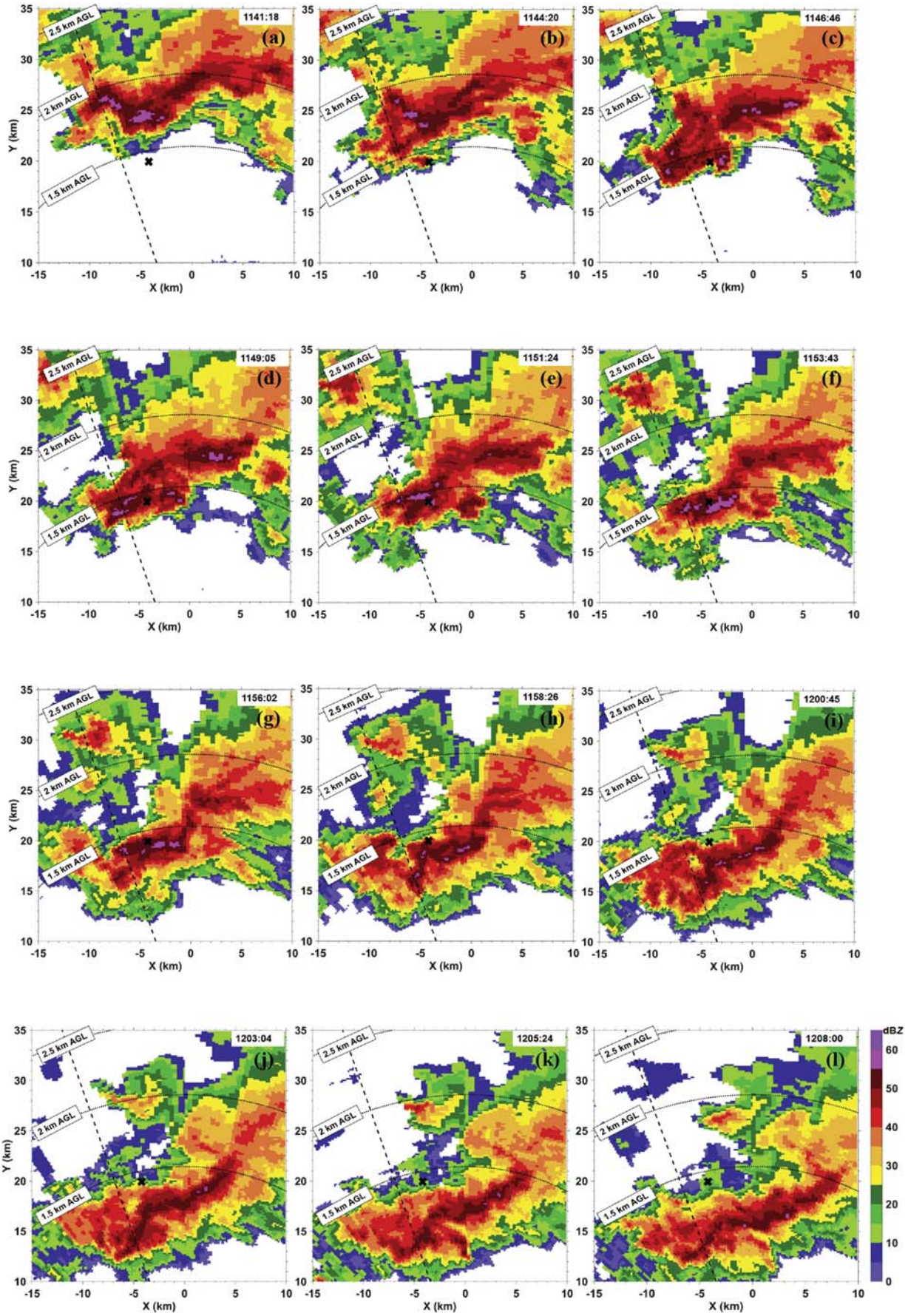

(caption on next page)

Fig. 2. Z_H PPIs (elevation angle 4°) on 5 Aug 2017 from 1141:18 to 1208:00 UTC (a) 1141:18, (b) 1144:20, (c) 1146:46, (d) 1149:05, (e) 1151:24, (f) 1153:43, (g) 1156:02, (h) 1158:26, (i) 1200:45, (j) 1203:04, (k) 1205:24, and (l) 1208:00. The dashed black lines indicate the azimuth of RHI, the black crosses indicate the location of HR station, and the dotted black lines indicate the altitude (AGL, south to north 1.5, 2, and 2.5 km, respectively).

On the evening of 5 August 2017, hailstorms crossed Beijing. Surface hail occurred during this process, and the storm ended at approximately 1400:00. The severe weather spotter of the HR station observed the surface hail from 1155:00 to 1200:00, with a maximum hail diameter of approximately 12 mm and a weight of approximately 1 g, which is a typical small hail. Fig. 2 shows that from 1141:18 to 1208:00, the core of this hailstorm moved from northwest to southeast, passing over the HR station (the parts of this hailstorm over the HR station in these PPIs are less than 1.5 km AGL). Parts of this hailstorm in PPIs are all below 2.5 km AGL, and the maximum Z_H exceeds 55 dB*Z*. At 1144:20, 1146:46, 1149:05, 1151:24, 1153:43, 1156:02 and 1158:26, the maximum values of Z_H exceed 40 dB*Z* over the HR station. This indicates that small hailstones may occur during this period from the perspective of Z_H.

4. Results and discussion

4.1. HID results and hail verification

To more accurately identify hailstones and confirm whether the identified hailstones results are consistent with the HR station real surface hail record, the improved HID method used in this study was applied to identify hydrometeors for IAP X-pol observations from 1141:18 to 1208:00, and the results are shown in Fig. 3. A large number of hailstones moved from northwest to southeast of the HR station. Since all observations were below 2.5 km AGL during this period (this altitude was much lower than the environmental 0 °C layer (~4.3 km AGL)), hydrometeors of HID results only comprise RH, RN and DZ particles. HID results showed that RH appeared over the HR station during time periods of 1151:24, 1153:43 and 1156:02. The RH occurrence location in the HID results is consistent with the real surface hail record at the HR station, but the occurrence time of RH in the HID results is earlier than the real surface hail record (1155:00 to 1200:00) at the HR station. The lag time is caused by it takes for the hail in the HID results (approximately 1.5 km AGL) to reach the ground from being in the air. In general, the validation result of hailstones is similar to the work for validation of polarimetric hail detection conducted by Heinselman and Ryzhkov (2006), these hailstones of identifying by the HID method corresponding to the real surface hail record; the HID method based on IAP X-pol is credible for hailstones identification in this study.

Furthermore, we also analyzed the HID results for the vertical section of this hailstorm along an azimuth angle of 341° (Fig. 4e). From the perspective of the overall distribution of hydrometeors in this hailstorm, in the nonmixed phase region, the hydrometeors are clearly layered, the CR particles are similar to VI particles and basically in the uppermost layer of the cloud body. The distribution height exceeds the environmental −10 °C layer. AG particles are mainly located in the marginal echo area where the hailstorm is weak, with a height of ~4 to 7 km. RN particles and DZ particles are below the environmental 0 °C layer, and LDG/HDG particles are distributed in the core of convection. LDG particles (above the environmental −10 °C layer) are higher than HDG particles (basically lower than the environmental −10 °C layer). Above the 0 °C layer, RH particles are basically in the mixed phase region and correspond to the strongest echo center, which is in line with the polarization characteristics of the rain-hail mixture particles. These distribution characteristics of hydrometeors in the vertical direction for this hailstorm are basically consistent with the identification results in Dolan and Rutledge (2009), and the distribution of the RH particles is also consistent with theoretical characteristics (Keenan, 2003).

4.2. Identification of the local mixed phase region

In this hailstorm, the IAP X-pol collected continuous high-resolution RHI data (azimuth angle 341°, dashed black lines in Fig. 2), the time interval was approximately 2 min, the elevation angle ranged from 0° to 30°, and the entire period contained times of 1145:55, 1148:14, 1150:33, 1152:53, 1155:11, 1157:36, 1159:55, 1202:14, 1204:33, 1207:09, 1209:29, and 1211:48. This phase includes the mature phase (1145:55 to 1150:33) and the dissipation phase (1152:53 to 1211:48), which are defined by the echo characteristics. Using the method of identifying mixed phase regions in *2.1. Input variables*, the local mixed phase region in this cell (the cell is at a distance of ~15 to 25 km at 1145:55) is defined as the dotted area shown in Fig. 4a; the black dotted area indicates the type I mixed phase region, and the blue dotted area indicates the type II mixed phase region. From the perspective of Z_H (the shaded area is the filled clutter of the cell's rear, which is not considered in this study), the echo top of this cell is just above the environmental −38 °C layer, the core of cell substantially reaches the height of the −38 °C layer, and the echo top of this cell bulges. These characteristics indicate that the cell is in the mature phase. The local mixed phase region contains almost all values of $Z_H \geq 50$ dB*Z* above the environmental 0 °C layer, which indicates that the local mixed phase region is mainly composed of larger particles. In addition, the type I mixed phase region is more inclined to the rear of this cell than the type II mixed phase region. The horizontal width of the K_{DP} column (black curve) is wider than that of the Z_{DR} column (green curve), and the height is roughly the same at this time. The local mixed phase region contains a Z_{DR}, K_{DP} column. Hydrometer identification results by HID (Fig. 4e) show that there are two liquid water-rich (LWR) areas in the local mixed phase region: one area is in the Z_{DR}, K_{DP} column (consistent with a large number of previous observation studies, e.g., Caylor and Illingworth, 1987; Hall et al., 1980, 1984; Illingworth et al., 1987) and the other area is located at ~22 to 24 km and at altitudes of ~5.5 to 7.5 km AGL. The liquid water content here is even richer than that in the Z_{DR}, K_{DP} column. In addition, the polarization characteristics of this area also show that liquid water is indeed most likely to exist (Z_{DR}, K_{DP} both show positive values in this area). Notably, the latter LWR area only existed at two moments, 1145:55 and 1148:14, and then, it disappeared (discussion in Section 4.3).

As mentioned above, the identification of the local mixed phase region added in the HID method in this study corrected the unreasonable hydrometeors layered phenomenon at the local mixed phase region of directly utilizing a hard threshold of environmental temperature to limit the distribution of hydrometeors (Fig. 4f), which allowed the HID results to observe more details of cloud microphysical processes inside storms, especially the role of supercooled water in storms.

4.3. Evolution of hail during the mature and dissipation phases of the cell

The hail area evolution is examined through continuous high-resolution RHI data collected by IAP X-pol based on HID results, which can indicate changes in the number of hail. As shown in Fig. 5a, the hail exhibited a steady decreasing trend beginning at 1148:14 and almost disappeared at 1211:48. To explain this hail evolution, seven features of this cell are examined: the height and width of the Z_{DR}, K_{DP} column, which is related to the intensity of storm updraft, supercooled water content, and the source of hail embryos; other features, such as the echo top height (ETH), the echo core top height ($Z_H \sim \geq 30$ dB*Z*) (CETH), and the mixed phase region height (MPH), are also examined. The results are shown in Fig. 5b. The features (ETH, CETH and MPH) of this cell all reveal that this cell strengthened steadily from 1145:55 to

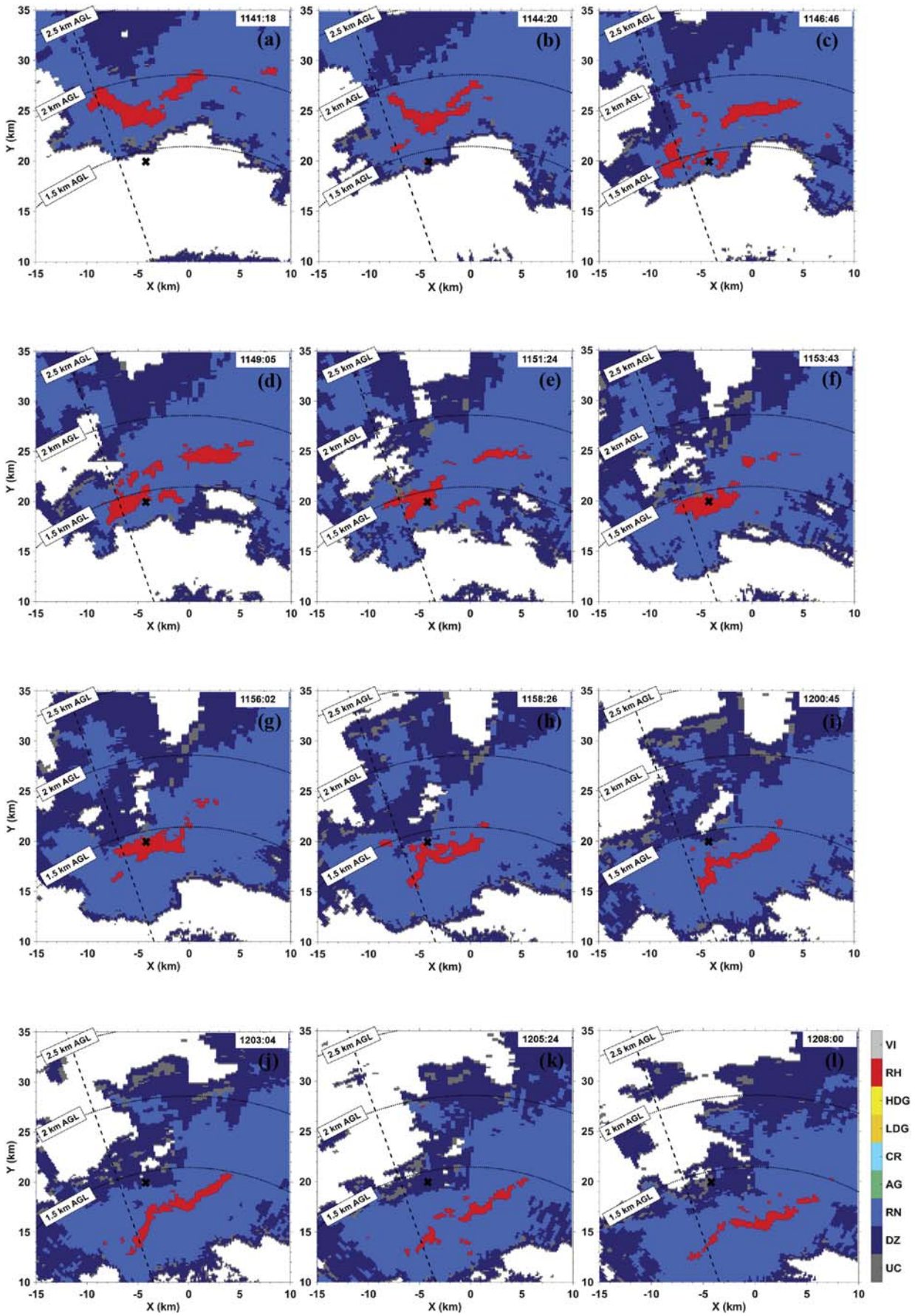

Fig. 3. The HID results are the same as those shown in Fig. 2.

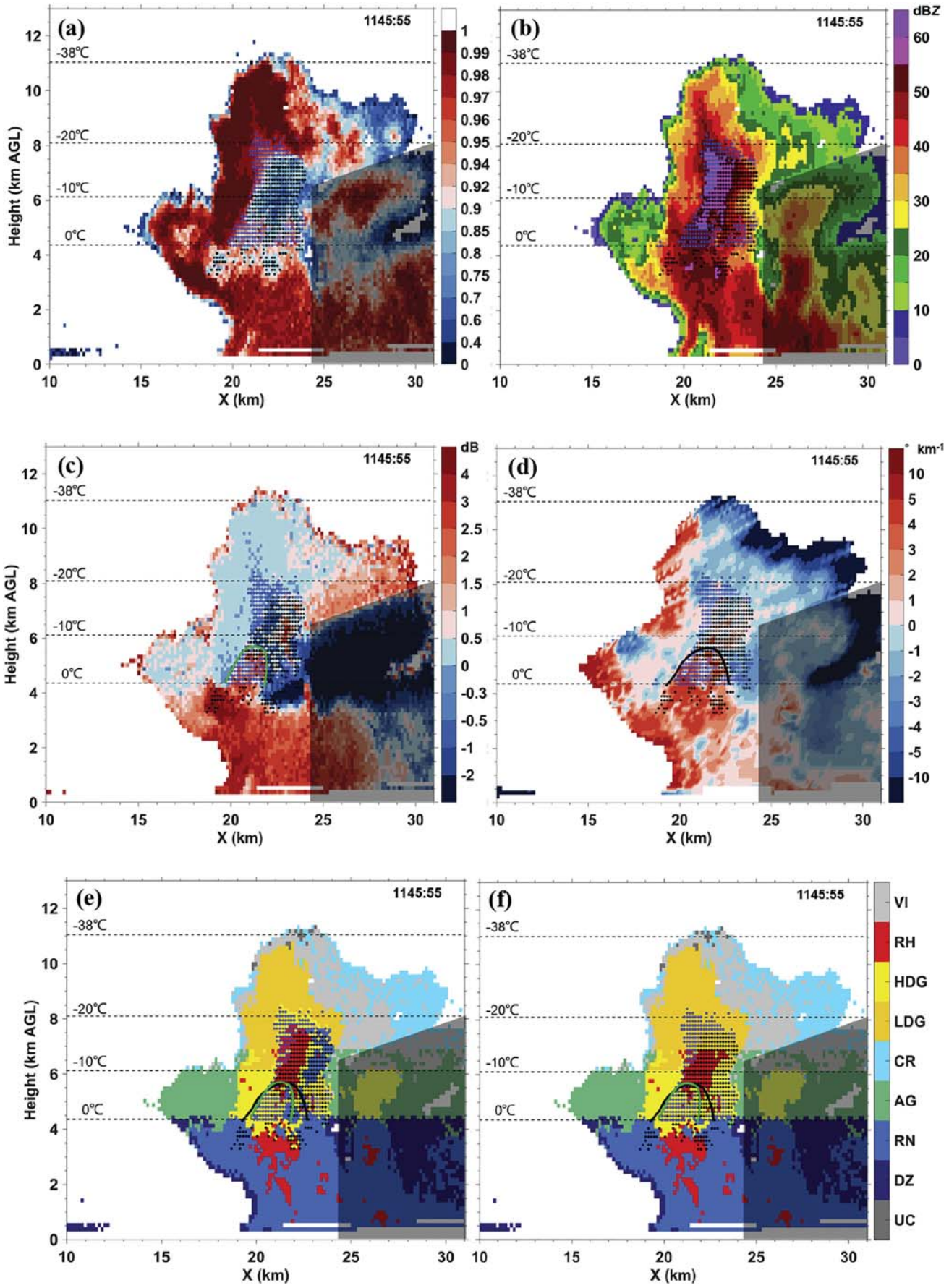

(caption on next page)

Fig. 4. 1145:55 UTC, (a) ρ_{HV}, (b) Z_H, (c) Z_{DR}, (d) K_{DP}, (e) HID result, and (f) HID result (Unimproved). The black dotted area indicates the type I mixed phase region, the blue dotted area indicates the type II mixed phase region, the green curve indicates the Z_{DR} column, the black curve indicates the K_{DP} column, the shaded area is the filled clutter of the cell's rear, and the dashed black lines indicate the environmental temperature altitude. (For interpretation of the references to colour in this figure legend, the reader is referred to the web version of this article.)

1150:33 and then quickly weakened. The Z_{DR} column changes in height and width remained basically the same as the three features of this cell before 1152:53, but subsequent evolution characteristics were significantly different (the K_{DP} column height and width changes are similar to the Z_{DR} column). The correlation coefficients between these seven features and the hail area are shown in Table 4. The correlation coefficient of the MPH is the highest, reaching 0.92, which also illustrates the importance of the local mixed phase region for the formation and growth of hail. Second, the CETH and ETH of this cell indicate that the evolution of hail is inseparable from the strength of the storm. The low correlation between the height and width of the Z_{DR}, K_{DP} column may be caused by the gradual forward shift in the updraft zone (discussion in detail below). However, notably, none of the features of this cell can explain the continuous decrease in hail since 1148:14.

To further understand this phenomenon, we checked the evolution of this cell during the period of 1145:55 to 1152:53 (Fig. 6). First, during this period, it is explicitly clear that the K_{DP} column is moving forward, which is consistent with the moving direction of this cell. Although there is no obvious forward movement of the Z_{DR} column, the range of the Z_{DR} column does expand forward, which means that as the cell moves, the Z_{DR}, K_{DP} column will also move with it (essentially the forward movement of the updraft zone). Second, there is a negative Z_{DR} zone of -2 to 0 dB (corresponding to $Z_H \sim \geq$ 50 dBZ) above the Z_{DR} column, hereafter known as the key area of hail (KAH). KAH has also been mentioned in previous observations (e.g., Kumjian et al., 2014, $Z_{DR} \sim$ -0.4 to -0.1 dB, $Z_H \sim >$ 60 dBZ), but in that study, the KAH only indicates the shaft of large hail, while in this study, we observed that the KAH not only comprises the shaft of hail at the lower layer of the KAH but also contains HDG particles at the upper layer of the KAH based on the HID results. Third, there are two LWR areas in the local mixed phase region: one area is inside the Z_{DR}, K_{DP} column (hereafter known as the LWR_A area), and the other is higher than the Z_{DR}, K_{DP} column; it adjoins the KAH and behind it (hereafter known as the LWR_B area). LWR_B only existed during the period of 1145:55 to 1148:14 and then disappeared from this cell (consistent with the time when the hail began to decrease). LWR_A continued to be maintained until the last stage of this cell (at 1207:09).

With the forward movement of the updraft zone, the K_{DP} column appears to be more sensitive to the forward movement of the updraft zone than the Z_{DR} column. At 1145:55, the KAH and LWR_B areas are mainly above the updraft zone. By 1148:14, both of them had been misaligned with the updraft zone and lagged behind it. At this time, the sedimentation of the HDG and RH particles at ~22 to 23.5 km has occurred since without updraft support (the Z_{DR} negative channel formed by the sedimentation of ice particles under the melting layer is particularly obvious). By 1150:33, the KAH is far from the updraft zone, and the LWR_B area almost disappeared. A large number of HDG and RH particles subsided below the melting layer at ~21 to 22 km, and the RH particles above the environmental 0 °C layer at the rear of this cell (~21 to 24 km) decreased significantly. Furthermore, at 1152:33, as a large amount of hydrometeors at the rear of this cell subsided to the ground, the height of the cloud body began to decline, and the KAH almost disappeared. In the subsequent period from 1155:11 to 1211:48, no KAH reappeared, except for a small KAH occurrence at 1159:55, but no LWR_B appeared at the rear, corresponding to a slight increase in hail displayed at 1202:14 and then continued to decrease until it almost disappeared within this cell at 1211:48.

Therefore, we concluded that the reduction in hail at 1148:14 and later was due to the forward shift in the updraft zone, which caused a large number of hailstones in the KAH to lose the support of the updraft and subside. Simultaneously, HDG particles in the upper layer of the KAH are most likely to be growing RH embryos with characteristics of high Z_H and negative Z_{DR}. In addition, these HDG particles may contain some smaller hailstones that cannot be identified as RH particles in this HID method. These RH embryos are located at a high altitude (approximately the environmental -20 °C layer), approximately 2 km away from the top of the Z_{DR}, K_{DP} column. Therefore, where do these RH embryos undergo wet growth and transform into the low layer RH of the KAH, in other words, where does supercooled water come from? First, the maximum diameter of surface hailstones in this hailstorm is

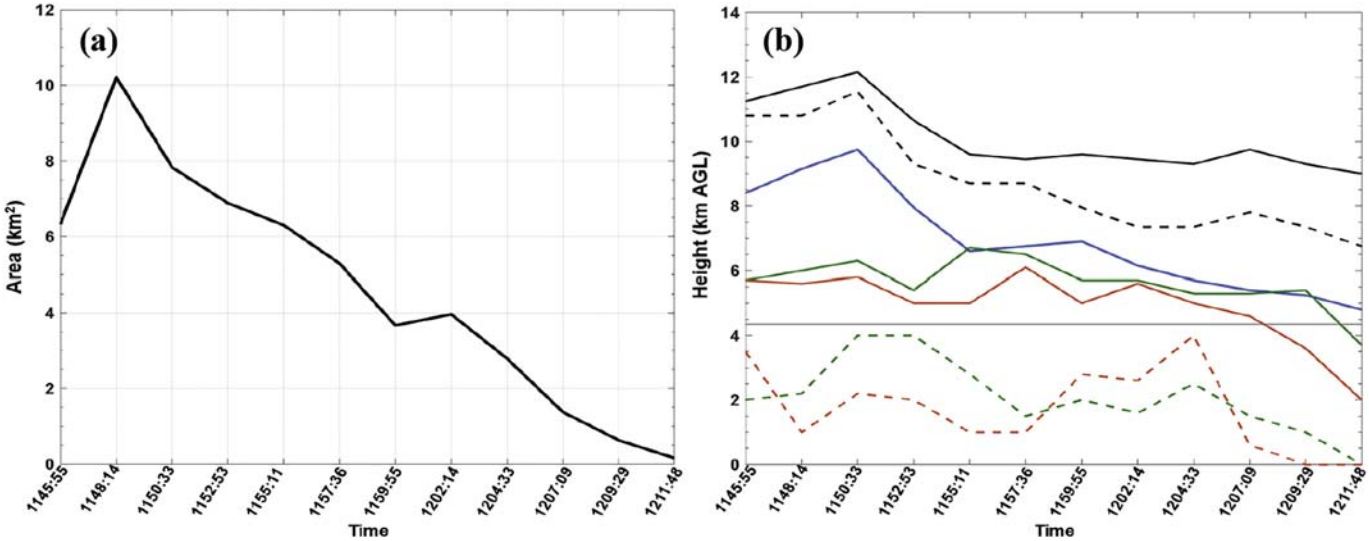

Fig. 5. 1145:55 to 1211:48 UTC, (a) hail area, (b) seven features of the cell (black line indicates the echo top height (ETH), dashed black line indicates the core echo top height (CETH), blue line indicates the local mixed phase region height (MPH), green line indicates the height of the Z_{DR} column, which is lower than the environmental 0 °C layer (gray line) at 1211:48, brown line indicates the height of the K_{DP} column, which is lower than the environmental 0 °C layer at 1209:29, dashed green line indicates the width of the Z_{DR} column, and dashed brown line indicates the width of the K_{DP} column). (For interpretation of the references to colour in this figure legend, the reader is referred to the web version of this article.)

Table 4
The correlation coefficients between seven features of this cell and hail area (bold means more than 98% confidence, * means more than 99% confidence, and all correlation coefficients exceed 95% confidence).

Parameters	Echo top height/Core Top height	Mixed phase region Height	Z_{DR} column height/ Width	K_{DP} column height/ Width
Correlation coefficients	**0.81***/ **0.87***	**0.92***	**0.66**/ **0.69**	**0.72***/ 0.26

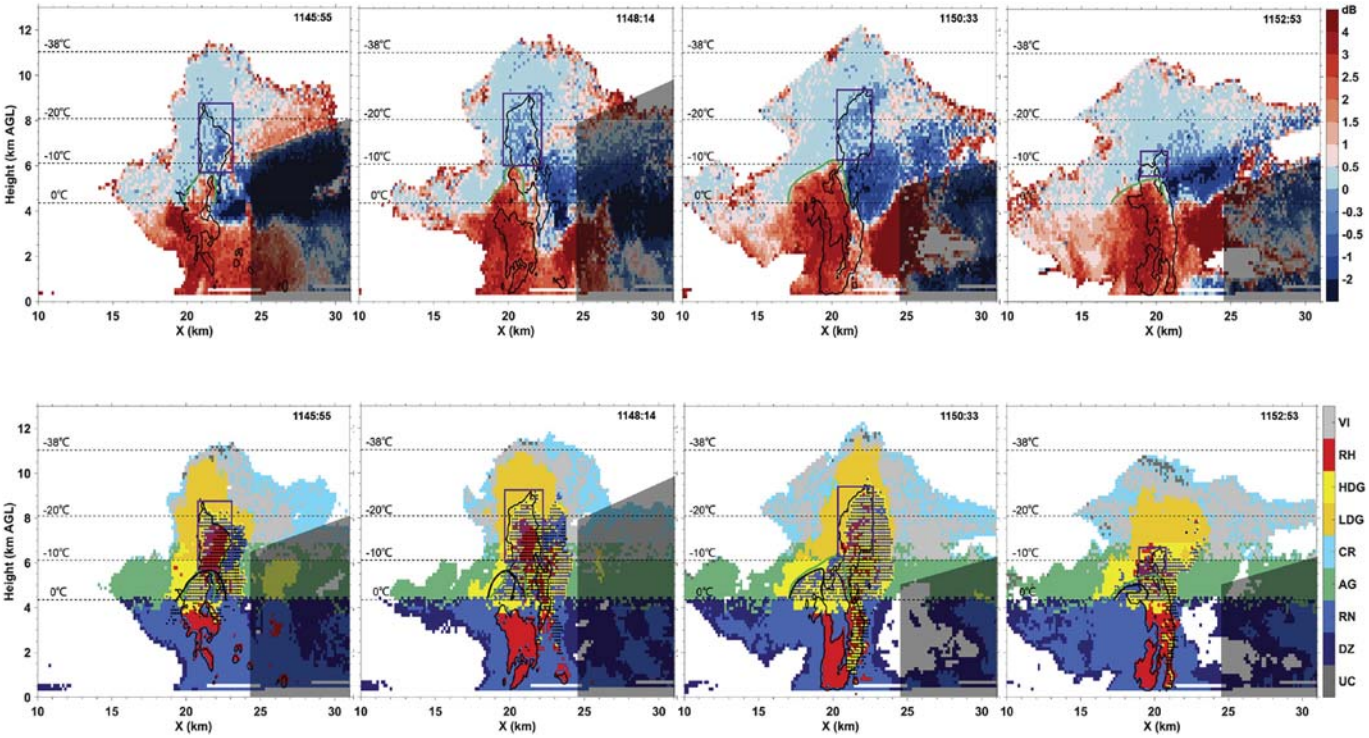

Fig. 6. The top row shows radar cross sections of Z_{DR} from 1145:55 to 1152:53 at an azimuth angle of 341°. The bottom row shows corresponding HID results, the black contours are the Z_H (50 dB*Z*), the purple squares indicate the KAHs, the green curves indicate the Z_{DR} columns, the black curves indicate the K_{DP} columns, the shaded area is the filled clutter of the rear of this cell, and the dashed lines indicate the environmental temperature altitude. (For interpretation of the references to colour in this figure legend, the reader is referred to the web version of this article.)

only 12 mm, which is considered to be small hail, and the updraft zone will gradually move forward with time, which cannot provide sufficient conditions to support the cyclic growth of hail (Browning and Foote, 1976; Conway and Zrnić, 1993). Second, when the updraft zone (indicated by the Z_{DR}, K_{DP} column) is strong and the location is aligned and below the KAH at 1145:55, the source of RH embryos is much higher than in the Z_{DR}, K_{DP} column. Therefore, these conditions within this cell suggest that RH embryos are unlikely to subside into the Z_{DR}, K_{DP} column to obtain the supercooled water required for wet growth. Furthermore, HID results at 1145:55 and 1148:14 show that there is another LWR area (LWR_B) at the same height as the KAH and just behind it. Thus, we speculate that the main supercooled water for the RH embryos with higher heights experiencing a wet growth source in the LWR_B. Later, larger hailstones that have experienced wet growth may fall to the lower layer of the KAH due to size sorting, and this part of hailstones may obtain supercooled water within the Z_{DR}, K_{DP} column and continue to grow. Note that the updraft zone indicated by the Z_{DR}, K_{DP} column is the main route for material transport in the storm (including the water vapor source); thus, the LWR_B area is a special supercooled water accumulative area in the upper layer of this cell formed by the water vapor source in the updraft zone.

5. Summary

In this study, an improved HID method for IAP X-pol was developed based on previous studies on the X-pol HID method (Dolan and Rutledge, 2009; Snyder et al., 2010). This modified HID method can more comprehensively identify hydrometeors in severe storms. In addition, the identification of local mixed phase regions in severe storms by ρ_{HV} improves the hard environmental temperature threshold of hydrometeors previously determined by the environmental temperature, which were directly obtained from the surface weather observatory soundings. And providing a possibility to observe the microphysical process of hailstones wet growth above the melting layer. This improved HID method was applied to one summer hailstorm over northern China on 5 August 2017, with data collected by mobile IAP X-pol. A simple verification was performed using the surface hailfall record provided by the National Weather Observatory of the CMA and the hailstones results identified by the HID method, which confirmed the reliability of this HID method in identifying hailstones. Furthermore, the evolutionary relationship between hail and the height and width of the Z_{DR}, K_{DP} column and other features of this cell, such as ETH, CETH, and MPH, were discussed. In addition, the K_{DP} column is more sensitive to the movement of the updraft zone than the Z_{DR} column in this cell, and we concluded that the location of the KAH and the updraft zone (indicated by the Z_{DR}, K_{DP} column) will determine the evolution of hail. Embryos of a large number of RH in the middle and lower layers of the KAH are most likely derived from HDG particles in the upper layer of the KAH, while the supercooled water for RH embryos and/or some smaller hail wet growth at higher altitudes originate from the LWR_B,

which is located at the same height as the KAH and just behind it.

Author contributions

Chuanhong Zhao, Yijun Zhang, and Yunjun Zhou conceived and designed this article; Chuanhong Zhao, Yijun Zhang, and Dong Zheng analyzed the data and wrote the paper; and Hui Xiao and Xiaoling Zhang supplied the analytical data. All authors have read and approved the final manuscript.

Declaration of Competing Interest

The authors declare that they have no conflicts of interest.

Acknowledgements

This research was supported by the National Natural Science Foundation of China (Grant no. 41875001, 41875169, 41675005, 41575037).

References

Balakrishnan, N., Zrnić, D.S., 1990. Use of polarization characterize precipitation discriminate large hail. J. Atmos. Sci. 47, 1525–1540. https://doi.org/10.1175/1520-0469(1990)047<1525:UOPTCP>2.0.CO;2.

Bechini, R., Chandrasekar, V., 2015. A semisupervised robust hydrometeor classification method for dual-polarization radar applications. J. Atmos. Ocean. Technol. 32, 22–47. https://doi.org/10.1175/JTECH-D-14-00097.1.

Bluestein, H.B., French, M.M., Tanamachi, R.L., Frasier, S., Hardwick, K., Junyent, F., Pazmany, A.L., 2007a. Close-range observations of tornadoes in supercells made with a dual-polarization, X-band, mobile doppler radar. Mon. Weather Rev. 135, 1522–1543. https://doi.org/10.1175/mwr3349.1.

Bluestein, H.B., Weiss, C.C., French, M.M., Holthaus, E.M., Tanamachi, R.L., Frasier, S., Pazmany, A.L., 2007b. The structure of tornadoes near Attica, Kansas, on 12 May 2004: high-resolution, mobile, doppler radar observations. Mon. Weather Rev. 135, 475–506. https://doi.org/10.1175/mwr3295.1.

Bringi, V.N., Chandrasekar, V., 2001. Polarimetric Doppler Weather Radar: Principles and Applications. Cambridge University Press, Cambridge, UK.

Bringi, V.N., Burrows, D.A., Menon, S.M., 1991. Multiparameter radar and aircraft study of raindrop spectral evolution in warm-based clouds. J. Appl. Meteorol. 30, 853–880. https://doi.org/10.1175/1520-0450(1991)030<0853:mraaso>2.0.co;2.

Bringi, V.N., Liu, L., Kennedy, P.C., Chandrasekar, V., Rutledge, S.A., 1996. Dual multiparameter radar observations of intense convective storms: the 24 June 1992 case study. Meteorog. Atmos. Phys. 59, 3–31. https://doi.org/10.1007/bf01031999.

Bringi, V.N., Knupp, K., Detwiler, A., Liu, L., Caylor, I.J., Black, R.A., 1997. Evolution of a Florida thunderstorm during the convection and precipitation/electrification experiment: the case of 9 August 1991. Mon. Weather Rev. 125, 2131–2160. https://doi.org/10.1175/1520-0493(1997)125<2131:eoaftd>2.0.co;2.

Browning, K.A., Foote, G.B., 1976. Airflow and hail growth in supercell storms and some implications for hail suppression. Q. J. R. Meteorol. Soc. 102, 499–533. https://doi.org/10.1002/qj.49710243303.

Caylor, I.J., Illingworth, A.J., 1987. Radar observations and modelling of warm rain initiation. Q. J. R. Meteorol. Soc. 113, 1171–1191. https://doi.org/10.1002/qj.49711347806.

Chandrasekar, V., Keränen, R., Lim, S., Moisseev, D., 2011. Recent advances in classification of observations from dual polarization weather radars. Atmos. Res. 119, 97–111. https://doi.org/10.1016/j.atmosres.2011.08.014.

Conway, J.W., Zrnić, D.S., 1993. A study of embryo production and hail growth using dual-doppler and multiparameter radars. Mon. Weather Rev. 121, 2511–2528. https://doi.org/10.1175/1520-0493(1993)121<2511:asoepa>2.0.co;2.

Dolan, B., Rutledge, S.A., 2009. A theory-based hydrometeor identification algorithm for X-band polarimetric radars. J. Atmos. Ocean. Technol. 26, 2071–2088. https://doi.org/10.1175/2009jtecha1208.1.

Feng, L., Xiao, H., Wen, G., Li, Z., Sun, Y., Tang, Q., Liu, Y., 2016. Rain attenuation correction of reflectivity for X-band dual-polarization radar. Atmosphere 7, 164. https://doi.org/10.3390/atmos7120164.

Feng, L., Xiao, H., Sun, Y., 2018. A study on hydrometeor classification and application based on X-band dual-polarization radar measurements. Clim. Environ. Res. 23, 366–386. https://doi.org/10.3878/j.issn.1006-9585.2018.17131.

Feng, L., Xiao, H., Luo, L., 2019. Simulation of polarization characteristics and attenuation of dual-polarization rain-measuring radar with T-matrix Methods. Chin. J. Comput. Phys. 36, 189–202. https://doi.org/10.19596/j.cnki.1001-246x.7826.

Giangrand, S.E., Krause, J.M., Ryzhkov, A.V., 2008. Automatic designation of the melting layer with a polarimetric prototype of the WSR-88D radar. J. Appl. Meteorol. Climatol. 47, 1354–1364. https://doi.org/10.1175/2007JAMC1634.1.

Guo, X., Fu, D., Li, X., Hu, Z., Lei, H., Xiao, H., Hong, Y., 2015. Advances in cloud physics and weather modification in China. Adv. Atmos. Sci. 32, 230–249. https://doi.org/10.1007/s00376-014-0006-9.

Hall, M.P.M., Cherry, S.M., Goddard, J.W.F., Kennedy, G.R., 1980. Rain drop sizes and rainfall rate measured by dual-polarization radar. Nature 285, 195–198. https://doi.org/10.1038/285195a0.

Hall, M.P.M., Goddard, J.W.F., Cherry, S.M., 1984. Identification of hydrometeors and other targets by dual-polarization radar. Radio Sci. 19, 132–140. https://doi.org/10.1029/rs019i001p00132.

He, Y., Lv, D., Xiao, H., 2009a. Attenuation correction of radar differential reflectivity for X-band dual polarization radar. Plateau Meteorol. 28, 135–144 Doi:CNKI:SUN:GYQX.0.2009-03-016.

He, Y., Lv, D., Xiao, H., Lei, H., Liu, D., Duan, S., 2009b. Attenuation correction of reflectivity for X-band dual polarization radar. Chin. J. Atmos. Sci. 33, 1027–1037. https://doi.org/10.3878/j.issn.1006-9895.2009.05.13.

He, Y., Xiao, H., Lv, D., 2010. Analysis of hydrometeor distribution characteristics in stratiform clouds using polarization radar. Chin. J. Atmos. Sci. 34, 23–34. https://doi.org/10.3878/j.issn.1006-9895.2010.01.03.

Heinselman, P.L., Ryzhkov, A.V., 2006. Validation of polarimetric hail detection. Weather Forecast. 21, 839–850. https://doi.org/10.1175/WAF956.1.

Hu, Z., Liu, L., 2014. Applications of wavelet analysis in differential propagation phase shift data de-noising. Adv. Atmos. Sci. 31, 825–835. https://doi.org/10.1007/s00376-013-3095-y.

Hu, Z., Liu, L., Wang, L., 2012. A quality assurance procedure and evaluation of rainfall estimates for C-band polarimetric radar. Adv. Atmos. Sci. 29, 144–156. https://doi.org/10.1007/s00376-011-0172-y.

Hubbert, J., Bringi, V.N., Carey, L.D., Bolen, S., 1998. CSU-CHILL polarimetric radar measurements from a severe hail storm in eastern Colorado. J. Appl. Meteorol. 37, 749–775. https://doi.org/10.1175/1520-0450(1998)037<0749:ccprmf>2.0.co;2.

Illingworth, A.J., Goddard, J.W.F., Cherry, S.M., 1987. Polarization radar studies of precipitation development in convective storms. Q. J. R. Meteorol. Soc. 113, 469–489. https://doi.org/10.1002/qj.49711347604.

Johnson, D.A., Hallett, J., 1968. Freezing and shattering of supercooled water drops. Q. J. R. Meteorol. Soc. 94, 468–482. https://doi.org/10.1002/qj.49709440204.

Keenan, T.D., 2003. Hydrometeor classification with a C-band polarimetric radar. Aust. Meteorol. Mag. 52, 23–31.

Kouketsu, T., Uyeda, H., Ohigashi, T., Oue, M., Takeuchi, H., Shinoda, T., Tsuboki, K., Kubo, M., Muramoto, K.-I., 2015. A hydrometeor classification method for X-band polarimetric radar: construction and validation focusing on solid hydrometeors under moist environments. J. Atmos. Ocean. Technol. 32, 2052–2074. https://doi.org/10.1175/jtech-d-14-00124.1.

Kumjian, M.R., Ryzhkov, A.V., 2008. Polarimetric signatures in supercell thunderstorms. J. Appl. Meteorol. Climatol. 47, 1940–1961. https://doi.org/10.1175/2007jamc1874.1.

Kumjian, M.R., Ryzhkov, A.V., Melnikov, V.M., Schuur, T.J., 2010. Rapid-scan super-resolution observations of a cyclic supercell with a dual-polarization WSR-88D. Mon. Weather Rev. 138, 3762–3786. https://doi.org/10.1175/2010mwr3322.1.

Kumjian, M.R., Khain, A.P., Benmoshe, N., Ilotoviz, E., Ryzhkov, A.V., Phillips, V.T.J., 2014. The anatomy and physics of ZDR columns: investigating a polarimetric radar signature with a spectral bin microphysical model. J. Appl. Meteorol. Climatol. 53, 1820–1843. https://doi.org/10.1175/jamc-d-13-0354.1.

Lim, S., Chandrasekar, V., Bringi, V.N., 2005. Hydrometeor classification system using dual-polarization radar measurements: model improvements and in situ verification. IEEE Trans. Geosci. Remote Sens. 43, 792–801. https://doi.org/10.1109/tgrs.2004.843077.

Liu, H., Chandrasekar, V., 2000. Classification of hydrometeors based on polarimetric radar measurements: development of fuzzy logic and neuro-fuzzy systems, and in situ verification. J. Atmos. Ocean. Technol. 17, 140–164. https://doi.org/10.1175/1520-0426(2000)017<0140:cohbop>2.0.co;2.

Loney, M.L., Zrnić, D.S., Straka, J.M., Ryzhkov, A.V., 2002. Enhanced polarimetric radar signatures above the melting level in a supercell storm. J. Appl. Meteorol. 41, 1179–1194. https://doi.org/10.1175/1520-0450(2002)041<1179:eprsat>2.0.co;2.

Marzano, F.S., Scaranari, D., Celano, M., Alberoni, P.P., Vulpiani, G., Montopoli, M., 2006. Hydrometeor classification from dual-polarized weather radar: extending fuzzy logic from S-band to C-band data. Adv. Geosci. 7, 109–114. https://doi.org/10.5194/adgeo-7-109-2006.

Marzano, F.S., Scaranari, D., Montopoli, M., Vulpiani, G., 2008. Supervised classification and estimation of hydrometeors from C-band dual-polarized radars: a bayesian approach. IEEE Trans. Geosci. Remote Sens. 46, 85–98. https://doi.org/10.1109/tgrs.2007.906476.

Melnikov, V., Zrnic, D., Ryzhkov, A.V., Zahrai, A., Carter, J., 2009. Validation of attenuation correction at X band performed with collocated S-band polarimetric radar. In: Extended Abstracts, 34th Conference on Radar Meteorology. American Meteor Society, Williamburg, VA, pp. 11A.15.

Park, S.G., Bringi, V.N., Chandrasekar, V., Maki, M., Iwanami, K., 2005a. Correction of radar reflectivity and differential reflectivity for rain attenuation at X band. Part I: theoretical and empirical basis. J. Atmos. Ocean. Technol. 22, 1621–1632. https://doi.org/10.1175/jtech1803.1.

Park, S.G., Maki, M., Iwanami, K., Bringi, V.N., Chandrasekar, V., 2005b. Correction of radar reflectivity and differential reflectivity for rain attenuation at X band. Part II: evaluation and application. J. Atmos. Ocean. Technol. 22, 1633–1655. https://doi.org/10.1175/jtech1804.1.

Park, H.S., Ryzhkov, A.V., Zrnić, D.S., Kim, K.-E., 2009. The hydrometeor classification algorithm for the polarimetric WSR-88D: description and application to an MCS. Weather Forecast. 24, 730–748. https://doi.org/10.1175/2008waf2222205.1.

Pazmany, A.L., Mead, J.B., Bluestein, H.B., Snyder, J.C., Houser, J.B., 2013. A mobile rapid-scanning X-band polarimetric (RaXPol) doppler radar system. J. Atmos. Ocean. Technol. 30, 1398–1413. https://doi.org/10.1175/jtech-d-12-00166.1.

Raghavan, R., Chandrasekar, V., 1994. Multiparameter radar study of rainfall: potential application to area time integral studies. J. Appl. Meteorol. 33, 1636–1645. https://

doi.org/10.1175/1520-0450(1994)033<1636:mrsorp>2.0.co;2.
Ryzhkov, A.V., Zhuravlyov, V.B., Rybakova, N.A., 1994. Preliminary results of X-band polarization radar studies of clouds and precipitation. J. Atmos. Ocean. Technol. 11, 132–139. https://doi.org/10.1175/1520-0426(1994)011<0132:proxbp>2.0.co;2.
Schuur, T., Ryzhkov, A.V., Heinselman, P., Zrnić, D.S., Burgess, D., Scharfenberg, K., 2003. Observations and Classification of Echoes with the Polarimetric WSR-88D Radar [OL]. National Severe Storms Laboratory.
Smith, P.L., Musil, D.J., Detwiler, A.G., Ramachandran, R., 1999. Observations of mixed-phase precipitation within a CaPE thunderstorm. J. Appl. Meteorol. 38, 145–155. https://doi.org/10.1175/1520-0450(1999)038<0145:oomppw>2.0.co;2.
Snyder, J.C., Bluestein, H.B., Zhang, G., Frasier, S.J., 2010. Attenuation correction and hydrometeor classification of high-resolution, X-band, dual-polarized mobile radar measurements in severe convective storms. J. Atmos. Ocean. Technol. 27, 1979–2001. https://doi.org/10.1175/2010jtecha1356.1.
Snyder, J.C., Bluestein, H.B., Venkatesh, V., Frasier, S.J., 2013. Observations of polarimetric signatures in supercells by an X-band mobile doppler radar. Mon. Weather Rev. 141, 3–29. https://doi.org/10.1175/mwr-d-12-00068.1.
Snyder, J.C., Ryzhkov, A.V., Kumjian, M.R., Khain, A.P., Picca, J., 2015. A Z_{DR} column detection algorithm to examine convective storm updrafts. Weather Forecast. 30, 1819–1844. https://doi.org/10.1175/waf-d-15-0068.1.
Snyder, J.C., Bluestein, H.B., Dawson II, D.T., Jung, Y., 2017a. Simulations of polarimetric, X-band radar signatures in supercells. Part I: description of experiment and simulated ρ_{hv} rings. J. Appl. Meteorol. Climatol. 56, 1977–1999. https://doi.org/10.1175/jamc-d-16-0138.1.
Snyder, J.C., Bluestein, H.B., Dawson II, D.T., Jung, Y., 2017b. Simulations of polarimetric, X-band radar signatures in supercells. Part II: Z_{DR} columns and rings and K_{DP} columns. J. Appl. Meteorol. Climatol. 56, 2001–2026. https://doi.org/10.1175/jamc-d-16-0139.1.
Stolzenburg, M., Marshall, T.C., Krehbiel, P.R., 2015. Initial electrification to the first lightning flash in New Mexico thunderstorms. J. Geophys. Res. Atmos. 120, 253–276. https://doi.org/10.1002/2015jd023988.
Straka, J.M., Zrnić, D.S., Ryzhkov, A.V., 2000. Bulk hydrometeor classification and quantification using polarimetric radar data: synthesis of relations. J. Appl. Meteorol. 39, 1341–1372. https://doi.org/10.1175/1520-0450(2000)039<1341:bhcaqu>2.0.co;2.
Tang, Q., Xiao, H., Guo, C., Feng, L., 2014. Characteristics of the raindrop size distributions and their retrieved polarimetric radar parameters in northern and southern China. Atmos. Res. 135-136, 59–75. https://doi.org/10.1016/j.atmosres.2013.08.003.
Thompson, E.J., Rutledge, S.A., Dolan, B., Chandrasekar, V., Cheong, B.L., 2014. A dual-polarization radar hydrometeor classification algorithm for winter precipitation. J. Atmos. Ocean. Technol. 31, 1457–1481. https://doi.org/10.1175/jtech-d-13-00119.1.
Vivekanandan, J., Turk, J., Stephens, G.L., Bringi, V.N., 1990. Microwave radiative transfer studies using combined multiparameter radar and radiometer measurements during COHMEX. J. Appl. Meteorol. 29, 561–585. https://doi.org/10.1175/1520-0450(1990)029<0561:mrtsuc>2.0.co;2.
Vivekanandan, J., Ellis, S.M., Oye, R., Zrnic, D.S., Ryzhkov, A.V., Straka, J., 1999. Cloud microphysics retrieval using S-band dual-polarization radar measurements. Bull. Am. Meteorol. Soc. 80, 381–388. https://doi.org/10.1175/1520-0477(1999)080<0381:cmrusb>2.0.co;2.
Wakimoto, R.M., Bringi, V.N., 1988. Dual-polarization observations of microbursts associated with intense convection: the 20 July storm during the MIST project. Mon. Weather Rev. 116, 1521–1539. https://doi.org/10.1175/1520-0493(1988)116<1521:dpooma>2.0.co;2.
Wang, Y., Chandrasekar, V., 2009. Algorithm for estimation of the specific differential phase. J. Atmos. Ocean. Technol. 26, 2565–2578. https://doi.org/10.1175/2009jtecha1358.1.
Xue, M., 2016. Preface to the special issue on the “observation, prediction and analysis of severe convection of China” (OPACC) national “973” projec. Adv. Atmos. Sci. 33, 1099–1101. https://doi.org/10.1007/s00376-016-0002-3.
Zhao, C., Zhou, Y., Xiao, H., Zhao, P., Zhang, X., Hu, T., 2019. A study of method for filtering copolar differential phase of X-band dual-polarimetric Doppler weather radar. Chin. J. Atmos. Sci. 43, 285–296. https://doi.org/10.3878/j.issn.1006-9895.1805.17289.
Zrnic, D.S., Ryzhkov, A.V., 1999. Polarimetry for weather surveillance radars. Bull. Am. Meteorol. Soc. 80, 389–406. https://doi.org/10.1175/1520-0477(1999)080<0389:pfwsr>2.0.co;2.
Zrnić, D.S., Ryzhkov, A., Straka, J., Liu, Y., Vivekanandan, J., 2001. Testing a procedure for automatic classification of hydrometeor types. J. Atmos. Ocean. Technol. 18, 892–913. https://doi.org/10.1175/1520-0426(2001)018<0892:tapfac>2.0.co;2.